

Inverse bubbles from broken supersymmetry

Giulio Barni,^{1,*} Simone Blasi,^{2,†} and Miguel Vanvlasselaer^{3,‡}¹*Instituto de Física Teórica IFT-UAM/CSIC, Cantoblanco, E-28049, Madrid, Spain*²*Deutsches Elektronen-Synchrotron DESY, Notkestr. 85, 22607 Hamburg, Germany*³*Theoretische Natuurkunde and IIHE/ELEM, Vrije Universiteit Brussel,**& The International Solvay Institutes, Pleinlaan 2, B-1050 Brussels, Belgium*

Building upon the recent findings regarding inverse phase transitions in the early universe, we present the first natural realisation of this phenomenon within a supersymmetry-breaking sector. We demonstrate that inverse hydrodynamics, which is characterized by the fluid being sucked by the bubble wall rather than being pushed or dragged, is actually not limited to a phase of (re)heating but can also occur within the standard cooling cosmology. Through a numerical analysis of the phase transition, we establish a simple and generic criterion to determine its hydrodynamics based on the generalised pseudo-trace. Our results provide a proof of principle highlighting the need to account for these new fluid solutions when considering cosmological phase transitions and their phenomenological implications.

Introduction – Phase transitions (PTs) in the early universe plasma, usually called *cosmological* phase transitions, are fascinating phenomena. First order PTs (FOPTs) proceeding via the nucleation and expansion of bubbles of the true vacuum inside a sea of false vacuum are of particular interest as they can be at the origin of the matter-antimatter asymmetry of the universe (baryogenesis) [1–14], lead to the production of dark matter [15–27] and primordial black holes [28–32], and can be a powerful source of primordial gravitational waves (GWs) as well [33–37]. The broad program to discover and investigate a possible background of GWs by current experiments such as LIGO–Virgo–Kagra [38] and Pulsar Timing Arrays [39], as well as future detectors such as the LISA [40] and the Einstein Telescope [41], opens the unique opportunity of probing the existence of FOPTs and of new fundamental physics. Indeed, FOPTs appear naturally in a large variety of scenarios beyond the Standard Model (BSM) like composite Higgs [42–46], extended Higgs sectors [47–54], axion models [55, 56], dark Yang-Mills sectors [57, 58], $B - L$ breaking sectors [59, 60] and SUSY breaking sectors [61, 62], and may also be catalysed by impurities in the early universe, see e.g. [63–75], as well as occur in the late Universe in the core of neutron stars [69, 76–78].

The dynamics of FOPTs involve a non-trivial interplay between the bubble wall and the surrounding plasma, which is pivotal in determining the phenomenology of the PT including the GW emission. The hydrodynamical modes describing the bulk fluid motion in the background of an expanding bubble during a *direct* FOPT have been classified a long time ago [79–82]: they consist of detonations, hybrids and deflagrations. For all these solutions, the fluid is either dragged or pushed (or both)

by the bubble wall. The bulk fluid velocity is then always aligned with the wall velocity in the plasma frame[83]. In the case of the *inverse* PTs, the plasma is instead sucked *inside* the expanding bubble and the fluid flows in the opposite direction of the bubble wall motion [84, 85] (see also Ref.[86] for the case of droplet collapse). These solutions have been so far studied in the context of a (re)heating PT [84, 85, 87] where the temperature of the system increases with time, and thus have been associated to superheated bubbles, see also [88, 89].

In this Letter, we show that inverse hydrodynamics is actually not limited to the heating scenario mentioned above, but can instead take place during the standard cooling of the universe as well. Remarkably, we find the emergence of this novel hydrodynamics during a seemingly standard, symmetry-breaking phase transition. This takes place within the context of dynamical supersymmetry (SUSY) and R -symmetry breaking, which represents the first explicit example for this class of FOPTs. Our findings extend the current understanding of what types of cosmological phase transitions can actually take place, thus opening up new directions for studying the corresponding GW signatures and other phenomenological aspects.

PTs in a SUSY breaking sector – Supersymmetry is not a symmetry of the low-energy theory. Therefore, if it is realised at high energy scales, it must be broken by a dedicated SUSY-breaking sector. A broad class of perturbative SUSY-breaking mechanisms can be described within the framework of an effective field theory that encapsulates the dynamics of the so-called *pseudomodulus*. This pseudomodulus corresponds to the scalar component x of the chiral superfield, X , which is directly related to SUSY breaking

$$X = \frac{x}{\sqrt{2}} e^{2ia/f_a} + \sqrt{2}\theta\tilde{G} + \theta^2 F, \quad (1)$$

where we have used the standard superspace notation. In our study, as a minimal benchmark model, we focus on

* giulio.barni@ift.csic.es

† simone.blasi@desy.de

‡ miguel.vanvlasselaer@vub.be

the O’Raifeartaigh model [90]. In addition to the *pseudomodulus*, the SUSY breaking sector contains four chiral superfields $\phi_1, \tilde{\phi}_1, \phi_2, \tilde{\phi}_2$. The superpotential takes the form

$$W = -FX + \lambda X \phi_1 \tilde{\phi}_2 + m(\phi_1 \tilde{\phi}_1 + \phi_2 \tilde{\phi}_2). \quad (2)$$

The model preserves a global $U(1)$ R -symmetry, which typically accompanies dynamical SUSY breaking [91, 92], and under which X has charge two, $R[X] = 2$. The vacuum expectation value (vev) of x is the order parameter for spontaneous R -symmetry breaking, while the additional scalar fields from ϕ_i and $\tilde{\phi}_i$ will have vanishing vev in all phases. The tree-level vacuum energy is $V_{\text{tree}}^{\text{min}} = |F|^2$ with x being a flat direction, indicating that supersymmetry is broken irrespectively of $\langle x \rangle$ while R -symmetry is preserved only at the origin, $\langle x \rangle = 0$.

The pseudomodulus flat direction is however lifted at the loop level, and the shape of the potential for x is controlled by the mass spectrum of the theory. One can see that this includes massive particles from the ϕ_i and $\tilde{\phi}_i$ superfields, with the scalar eigenstates split in pairs around the fermion ones, as well as massless fields from the superfield X corresponding to the pseudomodulus, x , the R -axion, a , and the goldstino, \tilde{G} . At one-loop, the potential for x acquires a global minimum at the origin, while remaining remarkably flat at large field values as a reflection of the underlying SUSY.

Finite-temperature effects, on the other hand, break SUSY explicitly and have a strong impact on the pseudomodulus effective potential. The typical thermal history of the minimal O’Raifeartaigh model considered here is then as follows [62, 93, 94]: at very high temperatures, $T \gtrsim \sqrt{F}$, the system has a single vacuum state, $\langle x \rangle = 0$, and R -symmetry is preserved. At lower temperatures, a new local minimum of the effective potential appears at relatively large field values, $\langle x \rangle / \sqrt{F} \gg 1$, which becomes the true vacuum of the theory below a certain critical temperature, T_c . This vacuum with broken R -symmetry will however become metastable and eventually disappear at even lower temperatures, given that the only minimum at zero temperature is at $\langle x \rangle = 0$.

Overall, the system undergoes two phase transitions, namely (1) the breaking of the R -symmetry at high temperatures and (2) its restoration at low temperatures, which turn out to be first order and governed by a thermal barrier. More details on the standard derivation of the effective potential for x and the associated thermal history can be found in App. C and references therein [95–97], as well as in Ref. [62].

In this paper, we will focus on the first transition that will take place in the expanding universe, namely the R -symmetry breaking FOPT: $\langle x = 0 \rangle \rightarrow \langle x \neq 0 \rangle$. As it turns out, this FOPT can actually proceed according to either the direct or the inverse hydrodynamics (the latter presented in Ref. [84, 85]) depending on the microscopic coupling constant λ entering the superpotential in

Eq. (2), while the second R -symmetry restoring FOPT will always be direct.

Thermodynamics and hydrodynamics of R -symmetry breaking – In the early universe, FOPTs can be modelled as the interplay between a scalar field ϕ , whose vacuum expectation value represents the order parameter of the transition, and the surrounding plasma which is often well described by a relativistic fluid. The energy-momentum tensor of the system consists then of those two contributions, $T^{\mu\nu} = T_{\text{fluid}}^{\mu\nu} + T_{\phi}^{\mu\nu}$, with

$$T_{\phi}^{\mu\nu} = \partial^{\mu}\phi\partial^{\nu}\phi - g^{\mu\nu} \left(\frac{1}{2}(\partial\phi)^2 - V(\phi) \right), \quad (3a)$$

$$T_{\text{fluid}}^{\mu\nu} = (e + p)u^{\mu}u^{\nu} - pg^{\mu\nu}, \quad (3b)$$

where u^{μ} is the four-velocity of the fluid, e is the energy density, p is the pressure and $V(\phi)$ is the scalar potential. The pressure is related to the free energy as $p = -\mathcal{F}$, while the energy and enthalpy density are given by

$$e = T \frac{dp}{dT} - p, \quad w = e + p = T \frac{dp}{dT}. \quad (4)$$

In any particle physics model that can be solved (even if only approximately, *e.g.* in a loop expansion), the free energy \mathcal{F} can be obtained directly from the effective potential at finite temperature, $V_0 + V_T \equiv \mathcal{F}$. Consequently, the knowledge of the free energy of a given theory allows us to compute all the thermodynamic quantities of interest without introducing a simplified Equation of State (EoS) for the fluid, such as for instance the bag EoS and its generalizations.

The conservation of the energy-momentum tensor across the phase boundary, $\nabla_{\mu}T^{\mu\nu} = 0$, gives the following relations between the velocities, the energies and the pressures [98]

$$v_+ v_- = \frac{p_+ - p_-}{e_+ - e_-}, \quad \frac{v_+}{v_-} = \frac{e_- + p_+}{e_+ + p_-}, \quad (5)$$

where the subscript “ \pm ” denotes quantities in front of/behind the phase boundary, so that for instance “ $-$ ” always represents the interior of the bubble.

We defined inverse PTs as transitions displaying negative bulk velocities in the plasma frame: rather than being pushed outward, the surrounding plasma is drawn inward, effectively being sucked into the expanding bubble. Let us now provide a sharper characterization, or criterion, of inverse hydrodynamics which extends the intuitive one put forward in Ref. [84], according to which inverse PTs are found when the transition proceeds against the vacuum energy (namely, the $T = 0$ effective potential for the order parameter). We find that a fully general characterization of inverse hydrodynamics can be obtained by defining a generalised pseudo-trace, α_{ϑ} , which indicates the strength of the phase transition and extends the definition within the bag EoS adopted in [84]

as well as the pseudo-trace, α_θ , introduced in [99],

$$\alpha_\theta \equiv \frac{4D\vartheta}{3w_+(T_+)} \equiv \frac{4\left(De(T_+) - \frac{\delta e}{\delta p}(T_+, T_-)Dp(T_+)\right)}{3w_+(T_+)}, \quad (6)$$

where the D and δ are defined as $Df = f_+(T_+) - f_-(T_+)$ and $\delta f = f_-(T_+) - f_-(T_-)$. For given values of T_\pm , they can be related to v_\pm via the matching conditions in (5), then, inverse hydrodynamics takes place for $\alpha_\theta < 0$, while the standard one is realised for $\alpha_\theta > 0$. In this way, we discover that PTs proceeding against the vacuum energy can nonetheless display direct hydrodynamics.

Notice that for relatively weak PTs with $T_+ \simeq T_-$, $\delta e/\delta p \simeq 1/c_{s,-}^2$, with $c_{s,-}$ being the speed of sound in the broken phase, Eq. (6) reduces to α_θ as defined in Ref. [99]. In the special case of a strictly constant speed of sound, one can refer to the template $\mu\nu$ model as introduced in Ref. [100] to capture deviations from the relativistic fluid with $c_s^2 \neq 1/3$. In this case, our definition further reduces to α_θ as derived within this template. Finally, when the speed of sound is $c_s^2 = 1/3$ as for a relativistic gas, this definition reduces to α_+ as considered in Ref. [84].

One can show that FOPTs with $\alpha_\theta = 0$ represent the limit of weak hydrodynamics, where $\Delta e = 0$ and $\Delta p = 0$, with $\Delta f = f_+(T_+) - f_-(T_-)$. By continuity, this is supposed to separate inverse from direct FOPTs.

Let us now examine the possible hydrodynamics of the R -symmetry breaking FOPT. The junction conditions above can be solved numerically by referring to the pressure and energy densities as evaluated directly from the free energy within our particle physics model. The allowed values for the (v_-, v_+) pairs are shown in Fig. 1 for a representative benchmark point. The matching conditions in Eq. (5) are solved for v_\pm in terms of the temperatures ahead and behind the wall, T_\pm . For consistency, we restrict T_+ to lie between T_c and the temperature when the barrier disappears, as this is the range for which the FOPT can actually take place. The various v_\pm trajectories in Fig. 1 are then shown together with the corresponding temperature T_+ according to the colour code. Because of the consistency condition on T_+ and the properties of our system free energy, the branches do not populate the entire $v_\pm \in (0, 1)$ parameter space. The regions corresponding to inverse and direct hydrodynamics, according to the sign of α_θ , are indicated by solid and dashed lines, respectively. We find that these regions remain neatly separated across the entire (v_-, v_+) plane, except for a small overlap in the regime of hybrid solutions (bottom-right corner). As a comparison, a similar discussion of the inverse branches in the case of the simplified (template) $\mu\nu$ -model is provided in Appendix A, where we find qualitative agreement with the full numerical study of the SUSY model presented here.

In the early universe, bubbles are efficiently formed when the nucleation rate catches up with the Hubble expansion. This condition, presented in more detail in

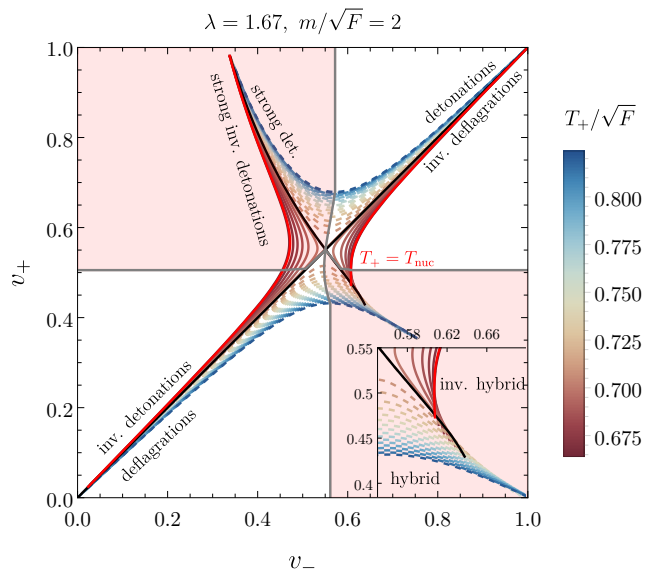


FIG. 1. Possible solutions to the fluid matching conditions for (v_-, v_+) for the R -symmetry breaking FOPT under consideration, plotting the relevant branches for different values of T_+ between T_c and the temperature where the barrier disappears. Dashed lines correspond to direct phase transitions, while solid lines indicate inverse transitions, as determined by the sign of α_θ . The solid red line highlights the relevant branch at T_{nuc} . The red-shaded area marks the region of strong (inverse) detonations and strong (inverse) deflagrations. In the bottom right corner, a zoomed-in view of the hybrid solution region reveals an overlap between different branches (see Appendix B for more details).

App. D and Refs. [101–106], connects the onset of the FOPT with a certain nucleation temperature, T_{nuc} . If we then further specify the temperature of the FOPT as T_{nuc} [107], we can select the bright red branch as the relevant one for this specific benchmark point. Notice that, as the matching conditions can not uniquely determine the bubble wall velocity, the actual value of v_\pm cannot be pinned down by the hydrodynamics only, and the full red branch can in principle be realised. On the other hand, when taking the wall velocity as an additional input, the fluid profile can be fully determined. As we can see, the FOPT within this benchmark point occurs in the inverse hydrodynamic regime.

In Fig. 2 we perform a scan over the model parameter space, by fixing $m/\sqrt{F} = 2$ and varying the coupling constant λ . The red line indicates the nucleation temperature, which always happens to be very close to the temperature where the barrier actually disappears.

For $\lambda \lesssim 1.63$, bubble nucleation occurs in the region where the hydrodynamics will be the one based on the (direct) detonation and deflagration types of solutions, while for $1.63 \lesssim \lambda \lesssim 1.68$ the hydrodynamics will be inverse. We can also notice that the condition of vanishing α_θ actually corresponds to the boundary between direct and inverse regions, which are determined

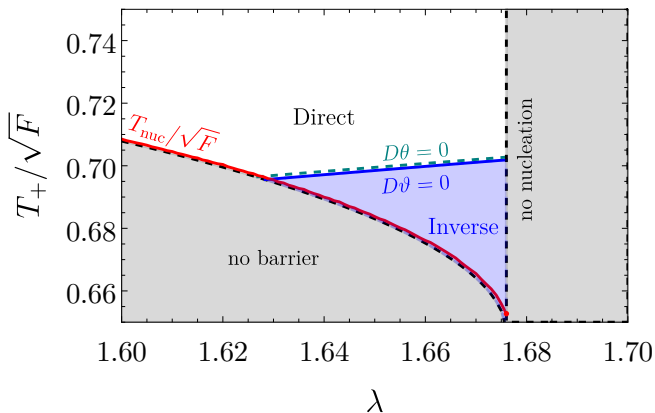


FIG. 2. The nucleation temperature (red line) is obtained as a function of λ by numerically solving the condition $S_3/T = 140$, which corresponds to setting $\sqrt{F} \sim \text{TeV}$ for concreteness (see App. D). The blue-shaded (white) region indicates the occurrence of the inverse (direct) FOPTs, whose boundary is shown according to the criteria $D\theta = 0$ and $D\phi = 0$. For this figure we fixed $m/\sqrt{F} = 2$.

independently by solving the fluid equations. As we can see, the approximate condition in terms of the pseudo-trace, $\alpha_\vartheta = 0$, reproduces this separation fairly well. This can be traced back to the fact that the speed of sound is not strongly temperature dependent in this model.

Inverse fluid solutions for R -symmetry breaking – The hydrodynamics of inverse PTs was presented for the first time in Ref. [84, 85] (see also [108]): there exist five different possible expansion modes with negative bulk velocities: i) inverse detonations (weak and Chapman-Jouguet (CJ)), ii) inverse deflagrations (weak and CJ), and iii) inverse hybrids.

This classification of hydrodynamic solutions was obtained within the (simplified) bag EoS. We have checked that this picture remains qualitatively the same also when considering the full form of the free energy (or effective potential) as evaluated explicitly for the SUSY model under consideration. In practice, we find only some quantitative differences related to the actual value of the speed of sound, which generally differs from $c_s^2 = 1/3$, and to the (mild) temperature dependence of c_s^2 , which requires solving the coupled system of fluid equations for the pressure and the energy density as discussed in Appendix (B). An example of the explicit profiles obtained by solving numerically the fluid equations for the benchmark point with $\lambda = 1.67$ and $m/\sqrt{F} = 2$ are shown in detail in Fig. 3 for an inverse detonation, together with the free energy of the system at the nucleation temperature showing the direction of the phase transition and a sketch of the bubble with the corresponding fluid profile.

Let us also mention that there is in principle the possibility that the bubble wall never reaches any of the steady states presented above, and keeps accelerating until bubbles collide, namely it runs away. Employing the

line of reasoning presented in Ref. [84], we find that the bubble never runs away in the model under consideration, and always reaches one of the steady states (see App. E and Refs. [109–111] for a derivation). Our hydrodynamic analysis however cannot determine which one of them, as mentioned above.

Coupling to the SM thermal bath – In the early universe, the SUSY breaking sector considered here is generally accompanied by additional spectator fields [112] that are in thermal equilibrium with the SUSY breaking sector and constitute a radiation bath. To assess the impact of these additional degrees of freedom, we redefine the energy and pressure as

$$p(T) \rightarrow p(T) + \tilde{c}^2 \tilde{a} T^4, \quad e(T) \rightarrow e(T) + 3\tilde{c}^2 \tilde{a} T^4, \quad (7)$$

where $\tilde{c}^2 = 1/3$, and \tilde{a} controls the number of the relativistic spectator degrees of freedom (dofs), which is expected to be $\tilde{a} \sim 70$ considering a supersymmetric extension of the Standard Model.

The presence of these fields will mostly influence the strength of the FOPT. In the limit $\tilde{a} \gg 1$, one has $\delta p/\delta e \simeq 1/3$ as expected for a gas of relativistic particles, and the generalised pseudo-trace in this limit becomes

$$\alpha_\vartheta \simeq \frac{4(De - 3Dp)}{3w_+(T_+)} \frac{1}{1+x}, \quad x = \frac{4\tilde{c}^2 \tilde{a} T_+^4}{w_+(T_+)}. \quad (8)$$

Thus, to a good approximation, the strength of the phase transition exhibits an inverse scaling with \tilde{a} , aligning with physical intuition. From explicit calculations, we find that the pseudo-trace and generalised pseudo-trace are always very close to each other in the parameter space of interest, and that the asymptotic behaviour in Eq. (8) is well established for $\tilde{a} \gtrsim 50$ leading to typical values of $\alpha_\vartheta \lesssim 10^{-2}$, while in the absence of spectator fields one would have $\alpha_\vartheta \lesssim 10^{-1}$.

In this regard, let us notice that there is in fact a fundamental difference between the strength of a standard (direct) FOPT and the case of an inverse FOPT. By referring to the definition of α_ϑ in Eq. (6), we can see that the part containing $Dp(T_+)$ will always contribute with a positive sign. This follows from the fact that the broken phase will necessarily have a larger pressure than the symmetric phase for the FOPT to take place and that $\delta e/\delta p \simeq 1/c_s^2$ is a positive quantity. Therefore, considering the case of negative α_ϑ , we can derive the following inequality:

$$\frac{3}{4} |\alpha_\vartheta| < \frac{\omega_-(T_+) - \omega_+(T_+)}{\omega_+(T_+)} = \frac{\Delta a_{\text{eff}}(T_+)}{a_{\text{eff},+}(T_+)}, \quad (9)$$

where $a_{\text{eff},+}(T_+)$ indicates the effective number of relativistic dofs in the symmetric phase at the temperature T_+ , according to the parametrization $3\omega(T)/4T^4 \equiv a_{\text{eff}}(T)$, and $\Delta a_{\text{eff}}(T_+)$ is the change in dofs in the broken phase at the same temperature. This relation shows that an inverse FOPT can be strong only when it involves a significant change in dofs

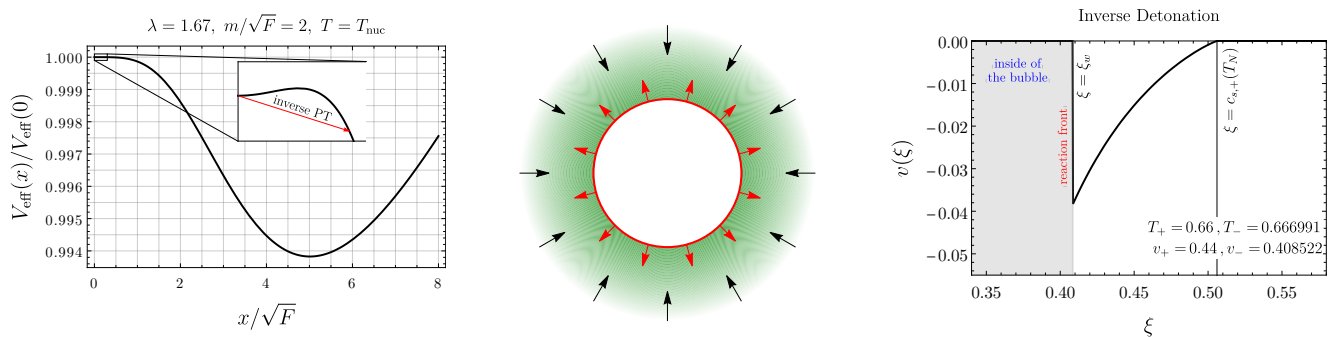


FIG. 3. Free energy of the system at finite temperature evaluated at one-loop at the nucleation temperature, with the arrow indicating the direction of the phase transition towards the minimum with a non-zero x (left panel), together with a sketch of the expanding bubble and its velocity in red, and the fluid profile in green (central panel) for a characteristic inverse detonation. The actual fluid profile in the plasma frame is shown in the right panel. Due to its inverse nature, the fluid velocity is always negative. See main text and Appendix B for details.

between the two phases. This is a structural property of the vacua of the theory under consideration, and it should be contrasted with the case of standard FOPTs whose strength is mostly controlled by the amount of supercooling that can be achieved in the expanding universe. In particular, Eq. (9) indicates that an inverse FOPT is not necessarily stronger when it becomes more supercooled.

Conclusion and outlook – We presented a simple SUSY breaking model displaying a window of *inverse* FOPTs during the spontaneous breaking of the R -symmetry. This represents the first explicit example of a BSM model leading to an inverse FOPT in a cooling cosmology, as well as a proof of principle for the relevance of this dynamics in the early universe.

We find that the sign of the generalised pseudo-trace, $\alpha_{\mathcal{J}}$ in Eq.(6), determines the *inverseness* of the transition. As a comparison, we also show that the sign of the pseudo-trace introduced in Ref. [99] offers a fair estimate for the type of the FOPT as well.

Our study motivates a broader investigation of inverse FOPTs in explicit BSM models. This includes establishing a deeper connection between the inverseness of a FOPT and its fundamental properties

and symmetries, exemplified here within a model of spontaneous SUSY breaking, as well as identifying possible non-SUSY realisations of this dynamics.

Finally, FOPTs are powerful sources of gravitational waves that can be detected at current and forthcoming GW observatories. This work provides motivation to characterize the GW spectrum related to inverse FOPTs, and to determine to which extent this can be distinguished from the one arising during direct FOPTs.

Acknowledgments – We sincerely acknowledge Thomas Konstandin, Xander Nagels, Alberto Mariotti, David Mateos, Diego Redigolo, and Mikel Sanchez-Garitaonandia for clarifying discussions and for reading the manuscript. GB is supported by the grant CNS2023-145069 funded by MICIU/AEI/10.13039/501100011033 and by the European Union NextGenerationEU/PRTR. GB also acknowledges the support of the Spanish Agencia Estatal de Investigacion through the grant “IFT Centro de Excelencia Severo Ochoa CEX2020-001007-S”. SB is supported by the Deutsche Forschungsgemeinschaft under Germany’s Excellence Strategy - EXC 2121 Quantum universe - 390833306. MV is supported by the “Excellence of Science - EOS” - be.h project n.30820817, and by the Strategic Research Program High-Energy Physics of the Vrije Universiteit Brussel.

-
- [1] V. A. Kuzmin, V. A. Rubakov, and M. E. Shaposhnikov *Phys. Lett. B* **155** (1985) 36.
 - [2] M. Shaposhnikov *JETP Lett.* **44** (1986) 465–468.
 - [3] A. E. Nelson, D. B. Kaplan, and A. G. Cohen *Nucl. Phys. B* **373** (1992) 453–478.
 - [4] M. Carena, M. Quiros, and C. E. M. Wagner *Phys. Lett. B* **380** (1996) 81–91, [[hep-ph/9603420](#)].
 - [5] J. M. Cline *Phil. Trans. Roy. Soc. Lond. A* **376** (2018), no. 2114 20170116, [[arXiv:1704.08911](#)].
 - [6] A. J. Long, A. Tesi, and L.-T. Wang *JHEP* **10** (2017) 095, [[arXiv:1703.04902](#)].
 - [7] S. Bruggisser, B. Von Harling, O. Matsedonskyi, and G. Servant *JHEP* **12** (2018) 099, [[arXiv:1804.07314](#)].
 - [8] S. Bruggisser, B. Von Harling, O. Matsedonskyi, and G. Servant *Phys. Rev. Lett.* **121** (2018), no. 13 131801, [[arXiv:1803.08546](#)].
 - [9] S. Bruggisser, B. von Harling, O. Matsedonskyi, and G. Servant *JHEP* **08** (2023) 012, [[arXiv:2212.11953](#)].
 - [10] D. E. Morrissey and M. J. Ramsey-Musolf *New J. Phys.* **14** (2012) 125003, [[arXiv:1206.2942](#)].
 - [11] A. Azatov, M. Vanvlasselaer, and W. Yin *JHEP* **10** (2021) 043, [[arXiv:2106.14913](#)].
 - [12] P. Huang and K.-P. Xie *JHEP* **09** (2022) 052, [[arXiv:2206.04691](#)].

- [13] I. Baldes, S. Blasi, A. Mariotti, A. Sevrin, and K. Turbang *Phys. Rev. D* **104** (2021), no. 11 115029, [arXiv:2106.15602].
- [14] E. J. Chun, T. P. Dutka, T. H. Jung, X. Nagels, and M. Vanvlasselaer arXiv:2305.10759.
- [15] A. Falkowski and J. M. No *JHEP* **02** (2013) 034, [arXiv:1211.5615].
- [16] I. Baldes, Y. Gouttenoire, and F. Sala *JHEP* **04** (2021) 278, [arXiv:2007.08440].
- [17] J.-P. Hong, S. Jung, and K.-P. Xie *Phys. Rev. D* **102** (2020), no. 7 075028, [arXiv:2008.04430].
- [18] A. Azatov, M. Vanvlasselaer, and W. Yin *JHEP* **03** (2021) 288, [arXiv:2101.05721].
- [19] I. Baldes, Y. Gouttenoire, F. Sala, and G. Servant *JHEP* **07** (2022) 084, [arXiv:2110.13926].
- [20] P. Asadi, E. D. Kramer, E. Kuflik, G. W. Ridgway, T. R. Slatyer, and J. Smirnov *Phys. Rev. D* **104** (2021), no. 9 095013, [arXiv:2103.09827].
- [21] P. Lu, K. Kawana, and K.-P. Xie *Phys. Rev. D* **105** (2022), no. 12 123503, [arXiv:2202.03439].
- [22] I. Baldes, Y. Gouttenoire, and F. Sala *SciPost Phys.* **14** (2023) 033, [arXiv:2207.05096].
- [23] A. Azatov, G. Barni, S. Chakraborty, M. Vanvlasselaer, and W. Yin *JHEP* **10** (2022) 017, [arXiv:2207.02230].
- [24] I. Baldes, M. Dichtl, Y. Gouttenoire, and F. Sala arXiv:2306.15555.
- [25] M. Kierkla, A. Karam, and B. Swiezewska *JHEP* **03** (2023) 007, [arXiv:2210.07075].
- [26] G. F. Giudice, H. M. Lee, A. Pomarol, and B. Shakya arXiv:2403.03252.
- [27] A. Azatov, X. Nagels, M. Vanvlasselaer, and W. Yin *JHEP* **11** (2024) 129, [arXiv:2406.12554].
- [28] H. Kodama, M. Sasaki, and K. Sato *Prog. Theor. Phys.* **68** (1982) 1979.
- [29] K. Kawana and K.-P. Xie *Phys. Lett. B* **824** (2022) 136791, [arXiv:2106.00111].
- [30] T. H. Jung and T. Okui arXiv:2110.04271.
- [31] Y. Gouttenoire and T. Volansky arXiv:2305.04942.
- [32] M. Lewicki, P. Toczek, and V. Vaskonen arXiv:2305.04924.
- [33] E. Witten *Phys. Rev.* **D30** (1984) 272–285.
- [34] C. J. Hogan *Mon. Not. Roy. Astron. Soc.* **218** (1986) 629–636.
- [35] A. Kosowsky and M. S. Turner *Phys. Rev.* **D47** (1993) 4372–4391, [astro-ph/9211004].
- [36] A. Kosowsky, M. S. Turner, and R. Watkins *Phys. Rev. Lett.* **69** (1992) 2026–2029.
- [37] M. Kamionkowski, A. Kosowsky, and M. S. Turner *Phys. Rev.* **D49** (1994) 2837–2851, [astro-ph/9310044].
- [38] A. Romero, K. Martinovic, T. A. Callister, H.-K. Guo, M. Martínez, M. Sakellariadou, F.-W. Yang, and Y. Zhao *Phys. Rev. Lett.* **126** (2021), no. 15 151301, [arXiv:2102.01714].
- [39] T. Bringmann, P. F. Depta, T. Konstandin, K. Schmidt-Hoberg, and C. Tasillo arXiv:2306.09411.
- [40] C. Caprini et al. *JCAP* **1604** (2016), no. 04 001, [arXiv:1512.06239].
- [41] **ET** Collaboration, M. Maggiore et al. *JCAP* **03** (2020) 050, [arXiv:1912.02622].
- [42] R. Pasechnik, M. Reichert, F. Sannino, and Z.-W. Wang *JHEP* **02** (2024) 159, [arXiv:2309.16755].
- [43] A. Azatov and M. Vanvlasselaer *JHEP* **09** (2020) 085, [arXiv:2003.10265].
- [44] M. T. Frandsen, M. Heikinheimo, M. Rosenlyst, M. E. Thing, and K. Tuominen *JHEP* **09** (2023) 022, [arXiv:2302.09104].
- [45] M. Reichert and Z.-W. Wang *EPJ Web Conf.* **274** (2022) 08003, [arXiv:2211.08877].
- [46] K. Fujikura, Y. Nakai, R. Sato, and Y. Wang *JHEP* **09** (2023) 053, [arXiv:2306.01305].
- [47] C. Delaunay, C. Grojean, and J. D. Wells *JHEP* **04** (2008) 029, [arXiv:0711.2511].
- [48] G. Kurup and M. Perelstein *Phys. Rev. D* **96** (2017), no. 1 015036, [arXiv:1704.03381].
- [49] B. von Harling and G. Servant *JHEP* **01** (2018) 159, [arXiv:1711.11554].
- [50] A. Azatov, D. Barducci, and F. Sgarlata *JCAP* **07** (2020) 027, [arXiv:1910.01124].
- [51] T. Ghosh, H.-K. Guo, T. Han, and H. Liu *JHEP* **07** (2021) 045, [arXiv:2012.09758].
- [52] M. Aoki, T. Komatsu, and H. Shibuya *PTEP* **2022** (2022), no. 6 063B05, [arXiv:2106.03439].
- [53] M. Badziak and I. Nalecz *JHEP* **02** (2023) 185, [arXiv:2212.09776].
- [54] U. Banerjee, S. Chakraborty, S. Prakash, and S. U. Rahaman arXiv:2402.02914.
- [55] L. Delle Rose, G. Panico, M. Redi, and A. Tesi *JHEP* **04** (2020) 025, [arXiv:1912.06139].
- [56] B. Von Harling, A. Pomarol, O. Pujolàs, and F. Rompineve *JHEP* **04** (2020) 195, [arXiv:1912.07587].
- [57] J. Halverson, C. Long, A. Maiti, B. Nelson, and G. Salinas *JHEP* **05** (2021) 154, [arXiv:2012.04071].
- [58] E. Morgante, N. Ramberg, and P. Schwaller *Phys. Rev. D* **107** (2023), no. 3 036010, [arXiv:2210.11821].
- [59] R. Jinno and M. Takimoto *Phys. Rev. D* **95** (2017), no. 1 015020, [arXiv:1604.05035].
- [60] A. Addazi, A. Marcianò, A. P. Morais, R. Pasechnik, J. a. Viana, and H. Yang *JCAP* **09** (2023) 026, [arXiv:2304.02399]. [Erratum: *JCAP* 03, E01 (2024)].
- [61] N. J. Craig arXiv:0902.1990.
- [62] N. Craig, N. Levi, A. Mariotti, and D. Redigolo *JHEP* **21** (2020) 184, [arXiv:2011.13949].
- [63] P. J. Steinhardt *Nucl. Phys. B* **190** (1981) 583–616.
- [64] Y. Hosotani *Phys. Rev. D* **27** (1983) 789.
- [65] U. A. Yajnik *Phys. Rev. D* **34** (Aug, 1986) 1237–1240.
- [66] K. Mukaida and M. Yamada *Phys. Rev. D* **96** (2017), no. 10 103514, [arXiv:1706.04523].
- [67] D. Canko, I. Gialamas, G. Jelic-Cizmek, A. Riotto, and N. Tetradis *Eur. Phys. J. C* **78** (2018), no. 4 328, [arXiv:1706.01364].
- [68] R. Jinno, T. Konstandin, H. Rubira, and J. van de Vis *JCAP* **12** (2021), no. 12 019, [arXiv:2108.11947].
- [69] R. Balkin, J. Serra, K. Springmann, S. Stelzl, and A. Weiler *SciPost Phys.* **14** (2023), no. 4 071, [arXiv:2105.13354].
- [70] P. Agrawal and M. Nee *SciPost Phys.* **13** (2022), no. 3 049, [arXiv:2202.11102].
- [71] S. Blasi and A. Mariotti *Phys. Rev. Lett.* **129** (2022), no. 26 261303, [arXiv:2203.16450].
- [72] P. Agrawal, S. Blasi, A. Mariotti, and M. Nee *JHEP* **06** (2024) 089, [arXiv:2312.06749].
- [73] R. Jinno, J. Kume, and M. Yamada *Phys. Lett. B* **849** (2024) 138465, [arXiv:2310.06901].
- [74] S. Blasi and A. Mariotti *SciPost Phys.* **18** (2025) 016, [arXiv:2405.08060].

- [75] S. Blasi, R. Jinno, T. Konstandin, H. Rubira, and I. Stomberg *JCAP* **10** (2023) 051, [arXiv:2302.06952].
- [76] R. Balkin, J. Serra, K. Springmann, S. Stelzl, and A. Weiler *JHEP* **06** (2022) 023, [arXiv:2106.11320].
- [77] J. Casalderrey-Solana, D. Mateos, and M. Sanchez-Garitaonandia arXiv:2210.03171.
- [78] R. Balkin, J. Serra, K. Springmann, S. Stelzl, and A. Weiler *JHEP* **02** (2025) 141, [arXiv:2307.14418].
- [79] M. Laine *Phys. Rev. D* **49** (1994) 3847–3853, [hep-ph/9309242].
- [80] H. Kurki-Suonio and M. Laine *Phys. Rev. D* **51** (1995) 5431–5437, [hep-ph/9501216].
- [81] M. Laine and K. Rummukainen *Nucl. Phys. B Proc. Suppl.* **73** (1999) 180–185, [hep-lat/9809045].
- [82] J. R. Espinosa, T. Konstandin, J. M. No, and G. Servant *JCAP* **1006** (2010) 028, [arXiv:1004.4187].
- [83] The plasma frame is defined as the frame in which the centre of the bubble is at rest.
- [84] G. Barni, S. Blasi, and M. Vanvlasselaer *JCAP* **10** (2024) 042, [arXiv:2406.01596].
- [85] Y. Bea, J. Casalderrey-Solana, D. Mateos, and M. Sanchez-Garitaonandia arXiv:2406.14450.
- [86] D. Cutting, E. Vilhonen, and D. J. Weir *Phys. Rev. D* **106** (2022), no. 10 103524, [arXiv:2204.03396].
- [87] M. A. Buen-Abad, J. H. Chang, and A. Hook *Phys. Rev. D* **108** (2023), no. 3 036006, [arXiv:2305.09712].
- [88] C. Caprini and J. M. No *JCAP* **01** (2012) 031, [arXiv:1111.1726].
- [89] J. B. Dent, B. Dutta, and M. Rai arXiv:2411.09757.
- [90] L. O’Raifeartaigh *Nucl. Phys. B* **96** (1975) 331–352.
- [91] A. E. Nelson and N. Seiberg *Nucl. Phys. B* **416** (1994) 46–62, [hep-ph/9309299].
- [92] K. A. Intriligator, N. Seiberg, and D. Shih *JHEP* **07** (2007) 017, [hep-th/0703281].
- [93] N. J. Craig, P. J. Fox, and J. G. Wacker *Phys. Rev. D* **75** (2007) 085006, [hep-th/0611006].
- [94] A. Katz *JHEP* **10** (2009) 054, [arXiv:0907.3930].
- [95] S. Coleman and E. Weinberg *Phys. Rev. D* **7** (Mar, 1973) 1888–1910.
- [96] M. Quiros, *Finite temperature field theory and phase transitions*, in *ICTP Summer School in High-Energy Physics and Cosmology*, pp. 187–259, 1, 1999. [hep-ph/9901312].
- [97] D. Curtin, P. Meade, and H. Ramani *Eur. Phys. J.* **C78** (2018), no. 9 787, [arXiv:1612.00466].
- [98] We remind that the velocities v_{\pm} have to be understood in the *front frame*, where the bubble wall is at rest.
- [99] F. Giese, T. Konstandin, and J. van de Vis *JCAP* **07** (2020), no. 07 057, [arXiv:2004.06995].
- [100] L. Leitao and A. Megevand *Nucl. Phys. B* **891** (2015) 159–199, [arXiv:1410.3875].
- [101] S. R. Coleman *Phys. Rev.* **D15** (1977) 2929–2936. [Erratum: *Phys. Rev.*D16,1248(1977)].
- [102] A. D. Linde *Phys. Lett.* **100B** (1981) 37–40.
- [103] A. D. Linde *Nucl. Phys.* **B216** (1983) 421. [Erratum: *Nucl. Phys.*B223,544(1983)].
- [104] J. Ellis, M. Lewicki, J. M. No, and V. Vaskonen *JCAP* **1906** (2019), no. 06 024, [arXiv:1903.09642].
- [105] A. H. Guth and S. H. H. Tye *Phys. Rev. Lett.* **44** (Apr, 1980) 963–963.
- [106] K. Enqvist, J. Ignatius, K. Kajantie, and K. Rummukainen *Phys. Rev.* **D45** (1992) 3415–3428.
- [107] The relation $T_{\text{nuc}} = T_{+}$ only holds for detonations and anti-deflagrations. For the other expansion modes, we still use this as a sensible approximation to identify the relevant v_{\pm} branch.
- [108] Y. Bea, M. Giliberti, D. Mateos, M. Sanchez-Garitaonandia, A. Serantes, and M. Zilhão arXiv:2412.09588.
- [109] W.-Y. Ai, B. Laurent, and J. van de Vis *JCAP* **07** (2023) 002, [arXiv:2303.10171].
- [110] W.-Y. Ai, B. Laurent, and J. van de Vis arXiv:2411.13641.
- [111] W.-Y. Ai, X. Nagels, and M. Vanvlasselaer *JCAP* **03** (2024) 037, [arXiv:2401.05911].
- [112] A spectator field does not change its physical properties, *e.g.* its mass, during the phase transition.
- [113] F. Giese, T. Konstandin, K. Schmitz, and J. van de Vis *JCAP* **01** (2021) 072, [arXiv:2010.09744].
- [114] M. Sanchez-Garitaonandia and J. van de Vis arXiv:2312.09964.
- [115] W.-Y. Ai, B. Garbrecht, and C. Tamarit *JCAP* **03** (2022), no. 03 015, [arXiv:2109.13710].

Appendix A: Inverse FOPTs in the $\mu\nu$ model

In this section, we examine the emergence of inverse phase transitions in the $\mu\nu$ -model [100], also referred to as the ν -model in Ref. [99] and the template model in Refs. [109, 113, 114]. The $\mu\nu$ -model extends the standard bag model by allowing the sound speed to deviate from the relativistic value of $1/\sqrt{3}$, while remaining constant within each phase. Explicitly, the EoS for the symmetric and broken phases is given by

$$e_{\pm}(T) = a_{\pm}T^{\nu_{\pm}} + \epsilon_{\pm}, \quad p_{\pm}(T) = c_{s,\pm}^2 a_{\pm}T^{\nu_{\pm}} - \epsilon_{\pm}, \quad \nu_{\pm} = 1 + 1/c_{s,\pm}^2. \quad (\text{A1})$$

In the following $\nu_{+} \equiv \nu$ and $\nu_{-} \equiv \mu$, we consider $\mu > \nu$ as this mimics the thermal history of the R -symmetry model, presented in the main text. The velocity relations from the matching conditions take the form

$$v_{+}v_{-} = \frac{\mu - \mu\nu - r\nu(3\alpha_{\theta} - 1)(\mu - 1)}{(\mu - \mu\nu + r\nu(3\alpha_{\theta} + \mu - 1))(\mu - 1)}, \quad \frac{v_{+}}{v_{-}} = \frac{(\mu - 1)(\mu - \mu\nu + r\nu(3\alpha_{\theta} - 1))}{\mu - \mu\nu - r\nu(3\alpha_{\theta} + \mu - 1)(\mu - 1)}, \quad (\text{A2a})$$

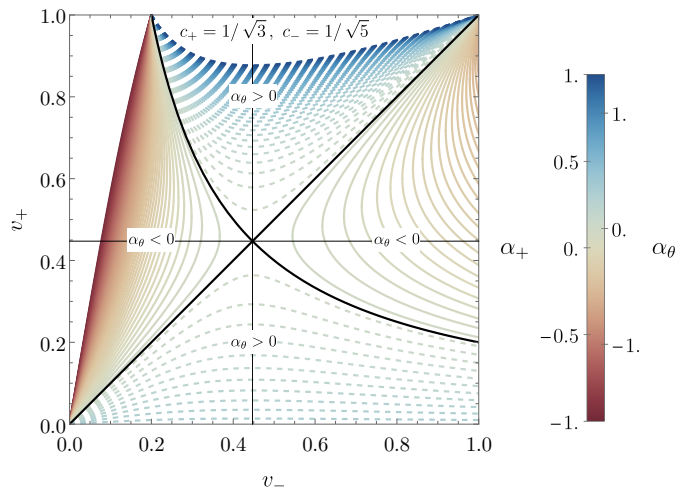


FIG. 4. Dashed (solid) lines represent direct (inverse) phase transitions. The inverse branches emerge as soon as $\alpha_\theta < 0$, whereas this is not necessarily the case for α_+ . The two strength parameters of the phase transition, α_+ and α_θ , coincide in the bag model when $\mu = \nu = 4$.

where we define the ratio $r \equiv a_+ T_+^\nu / a_- T_-^\mu$. Additionally, the strength parameter α_θ , defined from the pseudo-trace θ as $\alpha_\theta \equiv 4D\theta/3w_+$ where $\theta = e - p/c_{s,-}^2$, within the $\mu\nu$ model evaluates to

$$\alpha_\theta = \frac{\nu - 1}{3\nu} \left(\frac{\nu - \mu}{\nu - 1} + \mu\alpha_+ \right), \quad \alpha_+ \equiv \frac{\Delta\epsilon}{a_+ T_+^\nu} = \frac{\epsilon_+ - \epsilon_-}{a_+ T_+^\nu}. \quad (\text{A3})$$

It is important to emphasize that α_θ serves as the fundamental quantity determining the nature of the transition, and directly corresponds to the strength of the phase transition computed via the pseudo-trace.

Notably, in the case of the traditional bag EoS, where $\mu = \nu = 4$, the pseudo-trace coincides with the standard definition of the phase transition strength, $\alpha_\theta = \alpha_+$, thereby recovering the standard velocity relations.

It is shown in Fig. 4 that, as soon as $\alpha_\theta < 0$, the *inverse branches* emerge. This confirms that in the $\mu\nu$ -model, a negative α_θ implies an inverse phase transition. Analogously, for the bag EoS, a negative α_+ corresponds to an inverse PT. This result aligns with the characterization proposed in [84], where it was shown that within the bag EoS, $\Delta\epsilon < 0$ serves as a direct indicator of an inverse phase transition.

Appendix B: Solving the Hydrodynamic Equations for the Fluid Profiles

The conservation of the energy-momentum tensor for a relativistic fluid, given by $\nabla_\mu T^{\mu\nu} = 0$, yields two independent hydrodynamic equations. These equations can be rewritten in terms of the enthalpy density, $w = e + p$. We consider a spherically symmetric and self-similar configuration, where the fluid variables depend only on $\xi \equiv r/t$, the similarity variable. Using this variable, it can be shown that the hydrodynamics equations, in terms of the fluid velocity $v(\xi)$ and the fluid temperature $T(\xi)$, take the following form

$$(\xi - v) \frac{\partial_\xi T}{w} \frac{de}{dT} = \frac{2v}{\xi} + [1 - \gamma^2 v(\xi - v)] \partial_\xi v, \quad \frac{\partial_\xi T}{T} = \gamma^2 \mu(\xi, v) \partial_\xi v, \quad (\text{B1})$$

where $\mu(\xi, v) = \frac{\xi - v}{1 - \xi v}$. It is important to emphasize that the thermodynamic quantities, such as p and e , must be evaluated in the appropriate phase depending on the region where the equation is being solved. In the remainder of this section, we present the different types of expansion modes for inverse PTs within this general framework.

a. Inverse Deflagration To fully specify the system of equations in Eqs. (B1), we must define the initial conditions for $v(\xi)$ and $T(\xi)$. In the case of an inverse deflagration, this translates to

$$\xi_w = v_+, \quad v(\xi_w) = \mu(v_+, v_-), \quad T(\xi_w^+) = T_+, \quad T(\xi_w^-) = T_-, \quad (\text{B2})$$

where the $+$ phase corresponds to the false vacuum, while the $-$ phase corresponds to the true vacuum. Additionally, we impose the condition for the formation of a shock wave, which is given by $\mu(\xi_{sh}, v(\xi_{sh})) \xi_{sh} = c_{s,-}^2(T(\xi_{sh}))$. These initial conditions also apply to standard detonations, provided that the pair (v_+, v_-) satisfies the condition $v_+ > v_-$.

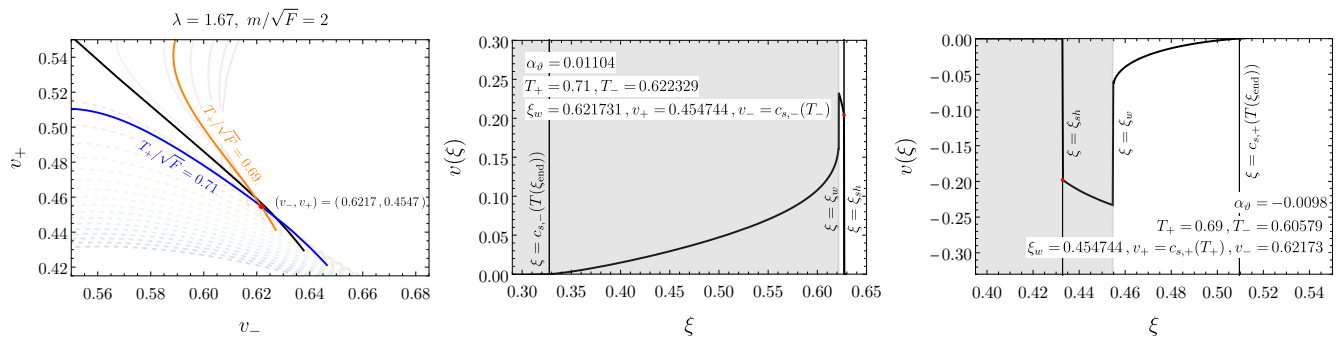


FIG. 5. Overlap of direct and inverse branches in the (v_-, v_+) plane and corresponding fluid profiles. *Left panel:* The (v_-, v_+) trajectories for different values of T_+ . The inverse branch is shown in orange, while the direct branch is displayed in blue. The highlighted crossing point indicates a case where both a direct and an inverse solution exist for the same (v_-, v_+) pair. *Middle panel:* Fluid profile corresponding to the direct hybrid solution. *Right panel:* Fluid profile for the inverse hybrid solution. The shaded regions indicate the interior of the bubble.

b. Inverse Detonations For inverse detonations, the initial conditions across the discontinuity translate into

$$\xi_w = v_-, \quad v(\xi_w) = \mu(v_-, v_+), \quad T(\xi_w^+) = T_+, \quad T(\xi_w^-) = T_-. \quad (\text{B3})$$

It can be checked directly that the rarefaction wave terminates at $\xi_{\text{end}} = c_{s,+}(T(\xi_{\text{end}}))$. For a standard detonation, the substitution $c_{s,+} \rightarrow c_{s,-}$ must be applied, as the rarefaction wave develops behind the reaction front, i.e., in the new phase.

These initial conditions also apply to standard deflagrations, provided that the pair (v_+, v_-) satisfies the appropriate conditions. In this case, the shock condition must be modified by replacing $c_{s,-}$ with $c_{s,+}$, as the shock forms ahead of the reaction front in the old phase.

Before discussing the last type of solution, it is important to highlight the presence of strong solutions in Fig. 5, where the red-shaded region indicates their domain. For (inverse) detonations/deflagrations, the strong regime is defined by the conditions $(v_+ \geq c_{s,+}(T_+))$ $v_- \leq c_{s,-}(T_-)$. As previously discussed in [84], strong (inverse) detonations cannot be consistently realised, while strong (inverse) deflagrations, although they may initially form due to the dynamics of the phase transition, are inherently unstable. Over time, they will decay into (inverse) hybrid solutions.

c. Inverse Hybrid For inverse hybrid solutions, as in the standard case, to make the profile stable, we must connect a strong inverse deflagration to a Chapman-Jouguet inverse detonation, which is defined as a detonation with $v_+ = c_{s,+}(T_+)$. The initial conditions then translate into

$$v(\xi_w^+) = \mu(\xi_w^+, c_{s,+}(T_+)), \quad v(\xi_w^-) = \mu(\xi_w^-, v_-), \quad T(\xi_w^+) = T_+, \quad T(\xi_w^-) = T_-, \quad (\text{B4})$$

where the four input parameters required to specify the system are (ξ_w, v_-, T_+, T_-) .

Additionally, the shock formation condition must be imposed, and one can verify that the rarefaction wave of the inverse detonation terminates again at $\xi_{\text{end}} = c_{s,+}(T(\xi_{\text{end}}))$. The maximal range of wall velocities for which an inverse hybrid solution exists is given by $c_{s,-}^2 < \xi_w < c_{s,+}$ where the lower bound arises because the slowest possible inverse hybrid is determined by the slowest possible shock.

For the case of a direct hybrid transition, a strong deflagration must instead be connected to a CJ detonation, where the latter is characterized by $v_- = c_{s,-}(T_-)$. The allowed range of wall velocities in this case is $c_{s,-} < \xi_w < 1$ where the upper bound is simply the speed of light, as there is no fundamental constraint on the maximum speed of the shock front.

d. Overlap in the hybrid corner In our numerical analysis, we observe that in the hybrid transition regime, the branches in the (v_-, v_+) plane exhibit an overlap between direct and inverse transitions. This is particularly evident when zooming in on the hybrid region, as shown in Fig. 5 (left panel). There, we explicitly construct two distinct solutions corresponding to the same pair of values (v_-, v_+) , demonstrating the existence of overlapping branches, in the middle and right panel of Fig. 5.

This overlap arises due to the stability conditions required for hybrid solutions. Specifically, for both direct and inverse hybrids to remain stable, the fluid velocity just behind (or in front of) the wall must match the local speed of sound in the respective phase at the corresponding temperature. That is, stability demands that for (inverse) hybrid holds $(v_+ = c_{s,+}(T_+))$ $v_- = c_{s,-}(T_-)$. This condition provides additional flexibility in setting $\xi_w = v_-$ for direct hybrids and $\xi_w = v_+$ for inverse hybrids, thus allowing both solutions to coexist.

Another key reason for this overlap is related to the structure of the separatrices (black solid lines) in the (v_-, v_+) plane. Ideally, these separatrices would be given by $v_- = v_+$ and $v_- v_+ = c_{s,-}^2$, however, since the speed of sound varies along the branches due to temperature dependence, the boundary between the direct and inverse solutions is no longer sharply defined. Despite their overlap in the (v_-, v_+) plane, the two solutions can still be distinguished physically. Each branch corresponds to a different set of temperatures (T_+, T_-) , leading to a different transition strength characterized by the generalised pseudotrace, α_θ , which will have in fact a different sign. Thus, even though the solutions may appear degenerate in velocity space, they remain distinct due to their thermodynamic properties.

Appendix C: Effective potential

In this appendix, we outline the computation of the one-loop and thermal corrections to the potential, as used in the main text.

a. One-Loop Potential. It is well known that quantum corrections at one loop modify the shape of the scalar potential [95]. At one loop, the tree-level potential is corrected by the *Coleman-Weinberg* potential, given by

$$V_{\text{CW}}(x) = \sum_{i=f,s} \frac{n_i (-1)^F}{64\pi^2} \left[M_i^4(x) \left(\log \frac{M_i^2(x)}{\Lambda^2} - \frac{3}{2} \right) \right], \quad (\text{C1})$$

such that the total *effective potential* is

$$V_0(x) = V_{\text{tree}}(x) + V_{\text{CW}}(x). \quad (\text{C2})$$

Here, $M_i(x)$ denotes the field-dependent masses of the particles in the spectrum, including the four fermionic and four scalar degrees of freedom. The sum runs over all states, with $F = 1(0)$ for fermions (scalars), and Λ is the renormalization scale, which we set to $\Lambda = m$.

b. Thermal corrections. In the early universe, high temperatures and the associated thermal fluctuations modify the effective potential. These thermal effects can be incorporated by adding finite-temperature corrections to the zero-temperature potential [96, 97], leading to

$$V_{\text{eff}}(T, x) = V_0(x) + V_T(x). \quad (\text{C3})$$

Here, $V_0(x)$ is the one-loop effective potential derived above, while the thermal potential $V_T(x)$ is given by

$$V_T(M_i(x)) = \sum_{i \in B} \frac{n_i}{2\pi^2} T^4 J_B \left(\frac{M_i^2(x)}{T^2} \right) - \sum_{i \in F} \frac{n_i}{2\pi^2} T^4 J_F \left(\frac{M_i^2(x)}{T^2} \right),$$

$$J_{B/F}(y^2) = \int_0^\infty dx x^2 \log \left[1 \mp \exp(-\sqrt{x^2 + y^2}) \right], \quad (\text{C4})$$

where the sum includes the (tree-level) massless fields in the X superfield corresponding to the goldstino, the pseudomodulus, and the R -axion, which will give a constant, namely x -independent, contribution to the free energy at one loop.

The full one-loop potential, including both quantum and thermal corrections, then takes the standard form

$$V_{\text{eff}}(x, T) = V_{\text{tree}}(x) + \sum_i [V_{\text{CW}}(M_i^2(x)) + V_T(M_i^2(x))] . \quad (\text{C5})$$

where we have neglected the thermal masses. In fact, perturbation theory for thermal field theory breaks down for massless particles. This breakdown can be avoided by the resummation of the so-called daisy diagrams, which amounts to add thermal masses to the tree-level ones in the CW and thermal potential. However, as our model does not contain dynamical massless particles on either phase, we expect this to be a good approximation. A detailed study of additional thermal effects is left for future work.

Appendix D: Nucleation theory

In this section we study the tunnelling rate for the R -symmetry breaking FOPT of interest. Starting with the effective potential derived in the previous section, we can proceed to the analysis of the phase transition. FOPTs

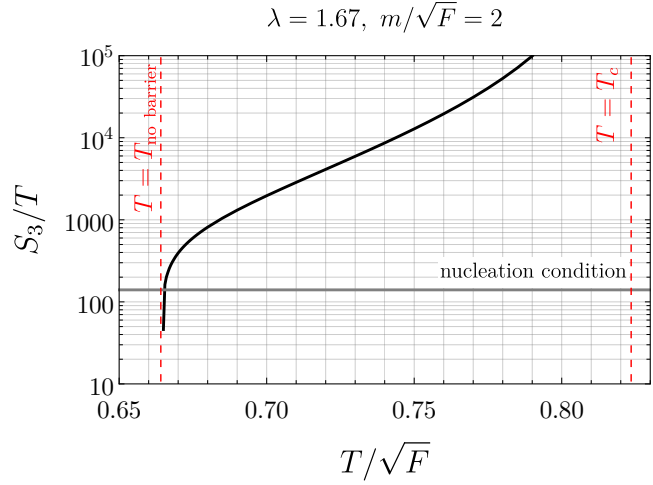


FIG. 6. We present the Euclidean action as a function of temperature for the benchmark point under consideration. Assuming a nucleation criterion of $S_3/T \sim 140$, this corresponds to setting $\sqrt{F} \sim \text{TeV}$. As we can see, tunnelling occurs around $T_{\text{nuc}}/\sqrt{F} \sim 0.665$.

occur when the minima of the effective potential corresponding to different phases are separated by a potential barrier, so that the transition proceeds via the nucleation of bubbles. The probability of bubble nucleation per unit time and unit volume is given by [101–103]

$$\Gamma(T) \simeq \Gamma_3 + \Gamma_4 = T^4 \left(\frac{S_3}{2\pi T} \right)^{3/2} e^{-S_3(T)/T} + \frac{1}{R_0^4} \left(\frac{S_4}{2\pi} \right) e^{-S_4}, \quad (\text{D1})$$

where S_3 and S_4 are the $O(3)$ and $O(4)$ bounce actions, respectively, and R_0 is the bubble radius at nucleation. In the case of interest, the tunnelling is dominantly induced by thermal fluctuations, and we can thus neglect the $O(4)$ contribution. The probability of finding a specific point of the universe in the false vacuum at a given temperature is given by [104, 105]

$$P_f(T) = \exp[-I(T)], \quad I(T) \equiv \frac{4\pi}{3} \int_T^{T_c} \frac{dT_1 \Gamma(T_1) v_w^3}{T_1^4 H(T_1)} \left[\int_T^{T_1} \frac{dT_2}{H(T_2)} \right]^3. \quad (\text{D2})$$

In Eq.(D1), the strongest dependence on the temperature comes from $\Gamma(T) \propto \exp(-S_3/T)$, so that the quantity $I(T)$ is mostly controlled by the ratio $\Gamma(T)/H(T)^4$, and one can estimate that, on average, one bubble has nucleated in one Hubble volume when $\Gamma(T) \sim H(T)^4$. The temperature that satisfies this condition is referred to as the nucleation temperature, T_{nuc} . The nucleation condition $\Gamma \sim H^4$ approximately reads

$$\left. \frac{S_3}{T} \right|_{T=T_{\text{nuc}}} \sim 4 \log \left(\frac{T_{\text{nuc}}}{H} \right) \sim 140, \quad (\text{D3})$$

where in the last step we have considered a FOPT occurring around $T_{\text{nuc}} \sim 1 \text{ TeV}$. One can additionally define the percolation temperature, T_{per} , as the temperature when a significant fraction of space, customarily taken to be $\sim 34\%$, has been converted to the true vacuum:

$$I(T \equiv T_{\text{per}}) = 0.34. \quad (\text{D4})$$

For relatively fast FOPTs, one however has $T_{\text{per}} \simeq T_{\text{nuc}}$.

The bounce solution and the corresponding bounce action are obtained via the well-known overshoot/undershoot method to solve the equations of motion for bubble nucleation. We present the value of the ratio S_3/T as a function of T in Fig.6 for the benchmark point with $\lambda = 1.67, m/\sqrt{F} = 2$ as in the main text.

Another important quantity characterising the FOPT is its duration, which is related to the radius of bubbles at collision, R_* , by the approximate relation [106]:

$$\frac{\beta}{H} \simeq \frac{(8\pi)^{1/3}}{R_* H}, \quad (\text{D5})$$

where β is given by

$$\beta \equiv -\frac{d}{dt} \frac{S_3}{T} \Big|_{T=T_{\text{nuc}}} = HT \frac{d}{dT} \frac{S_3}{T} \Big|_{T=T_{\text{nuc}}}. \quad (\text{D6})$$

For the FOPT under consideration, we find typical values of $\beta/H = \mathcal{O}(10^4)$ in the relevant parameter space. Given the short duration of the phase transition, the corresponding GW signal will be suppressed. We leave a comprehensive study of the model parameter space in view of the detectability of current and future GW experiments for future work.

Appendix E: Velocity of the bubble

Together with the strength, α_ϑ , the duration, β^{-1} , and the nucleation temperature, another crucial parameter for the description of the phase transition is the velocity of the bubble wall. In principle, there are two qualitatively different possibilities: 1) the bubble wall reaches a steady state, described by an (inverse) deflagration, (inverse) detonation or (inverse) hybrid or the bubble wall keeps accelerating until collision. The following study aims at clarifying which of the two is realised, following the methods presented in [84, 110, 111].

1. Collisionless regime computation

In principle, the possibility of runaway can be studied in the collisionless limit (see however [111]), since in this case, the wall boost factor becomes very large $\gamma_w \gg 1$, the pressure from the exchange of momentum originates from some particles losing their mass and inducing a kick on the wall. In the fast wall limit, no particle can escape the bubble, so we can consider only the entering species. To obtain the exchange of momentum, in the wall frame, we can apply the conservation of energy along the particle trajectory,

$$E_i = \sqrt{m_i^2 + p_{z,i}^2 + p_\perp^2}, \quad \frac{dE}{dz} = \left(\frac{dm_i^2}{dz} + \frac{dp_{z,i}^2}{dz} \right) \frac{1}{2E} = 0, \quad \Rightarrow \Delta p_{z,i}^{\text{part}} \approx -\frac{\Delta m_i^2}{2p_z}, \quad (\text{E1})$$

where Δm^2 has to be understood as the change of mass of the particle i upon crossing the wall. By conservation of momentum, the wall receives an equal and opposite kick, $\Delta p_z^{\text{part}} = -\Delta p_z^{\text{wall}} > 0$, which accelerates it forward or backwards depending on the sign of the kick. We observe that a particle *gaining* mass induces a negative kick, and so resists the expansion of the wall, while a particle *losing* mass aspires the wall. In the model under consideration, both types of particles are present, so the competition between them will determine the sign of the collisionless pressure. To capture the pressure induced by the plasma, we need to further convolute the momentum with the incoming flux

$$\mathcal{P}_{\text{plasma}} = \int dz \partial_z \phi \sum_i g_i \frac{dm_i^2(\phi)}{d\phi} \int \frac{d^3 \mathbf{p}}{(2\pi)^3 2E_i} f_i(p, z, T) \approx \sum_i g_i \int \frac{d^3 \mathbf{p}}{(2\pi)^3} \frac{\Delta m_i^2}{2E_i} f_{\text{outside}}^{\text{eq}}(p, T). \quad (\text{E2})$$

where the sum is to be performed over all particles which may lose or gain a mass across the bubble wall, and g_i is the number of dofs for each particle. By convention, a negative pressure aspires the wall while a positive one resists the expansion. The integral over the phase space is frame-independent and we compute it in the plasma frame. On the other hand, the force exerted by the vacuum energy is given by

$$F_{\text{vacuum}} \equiv \int dz \partial_z \phi \frac{dV^{T=0}(\phi)}{d\phi}, \quad (\text{E3})$$

Therefore, evaluating the pressure from Eq.(E2) in the limit $\gamma_w \rightarrow \infty$ if the following inequality is satisfied,

$$\mathcal{P}_{\text{plasma}}^{\gamma_w \rightarrow \infty} - F_{\text{vacuum}} < 0, \quad (\text{E4})$$

then the wall can in principle runaway. Numerical evaluation shows that for the inverse PT window studied in this paper, $F_{\text{bubble}} > 0$, implying that runaway is not possible.

2. Local thermal equilibrium approach

In the regime of very small velocities, one can approximate that the fluid inside the bubble wall can reach thermalisation, i.e. local thermal equilibrium [109, 111, 115]. In this case, the entropy current is conserved inside the wall as well and one can solve exactly the matching conditions. In this case, the pushing plasma effect is given by

$$\mathcal{P}_{\text{plasma}} \equiv - \int dz \partial_z \phi \sum_i \frac{dm_i^2(\phi)}{d\phi} \int \frac{d^3\mathbf{p}}{(2\pi)^3 2E_i} f_i(p, z, T) = \mathcal{P}_{\text{LTE}} + \mathcal{P}_{\text{dissipative}} . \quad (\text{E5})$$

In the LTE approach, we ignore the dissipative contributions. The approximate LTE expression becomes (when we can approximate $T_+ \approx T_-$):

$$F_{\text{vacuum}} - \mathcal{P}_{\text{plasma}} \approx \frac{3w_+}{4} \left(\frac{1}{4}(b-1) - |\alpha_+| \right), \quad b \equiv a_-/a_+, \quad (\text{E6})$$

where now $b > 1$. We observe that the driving force fuelling the expansion now originates from the change of d.o.f. and has to overcome the resisting force from the vacuum. For the case at hand, one can observe that $b \sim 2$, which suggests that, as $|\alpha_+|$ is always much smaller than $1/4$, the wall can expand within the LTE approach.

Combining the results from the Collisionless and LTE approach, one can expect the wall to reach a steady state rather than run away.
